J. Fluid Mech. (2002), *vol.* 454, *pp.* 203–233.
DOI: 10.1017/S0022112001007078 Printed in the United Kingdom

The velocity field under breaking waves: coherent structures and turbulence

By W. KENDALL MELVILLE, FABRICE VERON AND CHRISTOPHER J. WHITE†

Scripps Institution of Oceanography, University of California, San Diego, La Jolla, CA 92093-0213, USA

(Received 4 April 2000 and in revised form 25 August 2001)

Digital particle image velocimetry (DPIV) measurements of the velocity field under breaking waves in the laboratory are presented. The region of turbulent fluid directly generated by breaking is too large to be imaged in one video frame and so an ensemble-averaged representation of the flow is built up from a mosaic of image frames. It is found that breaking generates at least one coherent vortex that slowly propagates downstream at a speed consistent with the velocity induced by its image in the free surface. Both the kinetic energy of the flow and the vorticity decay approximately as t^{-1}. The Reynolds stress of the turbulence also decays as t^{-1} and is, within the accuracy of the measurements, everywhere negative, consistent with downward transport of streamwise momentum. Estimates of the mometum flux from waves to currents based on the measurements of the Reynolds stress are consistent with earlier estimates. The implications of the measurements for breaking in the field are discussed. Based on geometrical optics and wave action conservation, we suggest that the presence of the breaking-induced vortex provides an explanation for the suppression of short waves by breaking. Finally, in Appendices, estimates of the majority of the terms in the turbulent kinetic energy budget are presented at an early stage in the evolution of the turbulence, and comparisons with independent acoustical measurements of breaking are presented.

1. Introduction

An improved understanding of turbulence and mixing due to wave breaking is essential for progress in a number of areas of air–sea interaction. For surface waves, breaking is normally considered to be a sink of energy (and action); although, like any disturbance, it may also be a source. Breaking, as a dissipative mechanism when momentum is conserved, leads to the generation of currents. The details of the near-surface currents depend on the fact that breaking is a source of turbulence for the upper mixed layer, and may lead to departures from classical law-of-the-wall velocity profiles. Fluxes of heat and gas across the air–sea interface, which are so important for weather and climate up to global scales, depend on the levels of surface turbulence, which are due in part to breaking. Bubbles entrained by breaking may also contribute to gas transfer, and their contribution depends on the depths to which they are mixed by the surface currents and turbulence. Breaking provides strong signatures in remote

† Present address: Solar Turbines Inc., 9280 Sky Park Ct., San Diego, CA 92123 USA.

sensing of the ocean surface; signatures that depend on the processes of wave–current interaction associated with wave breaking. For these reasons and more, an improved knowledge of the fluid dynamics of breaking is vital to a better understanding of air–sea interactions from micro- to global scales (Banner & Peregrine 1993; Melville 1996).

While progress in measuring breaking and related wave and mixed-layer processes in the field has improved remarkably over the last decade, we are not yet at the stage where field measurements can match the quality, and they will never match the control, that is available in the laboratory. Furthermore, most field measurements, which are local, are unable to capture the evolution of the velocity field from the pre- to post-breaking states. Even identification of breaking in the field is difficult, since the smaller waves may break with no visible air entrainment. Thus, laboratory measurements are necessary to measure and understand the evolution of the velocity field under breaking waves.

Rapp & Melville (1990, hereinafter referred to as RM) using point-by-point laser-Doppler techniques and ensemble averaging over a number of realizations of the flow, had some success in measuring the turbulence generated by fully unsteady breaking waves in the laboratory. Using a wave focusing technique, they showed that Froude scaling, based on pre-breaking wave variables, and inertial models of the large-scale turbulence, described some of the gross features of the evolution of the flow. They found that the ensemble-averaged (mean) velocity displayed a coherent vortex decaying with time; that approximately 90% of the energy lost from the waves was dissipated within four wave periods, and that subsequently the kinetic energy decayed as t^{-1}. Subsequent measurements of the air entrained by breaking (Lamarre & Melville 1991) showed that the work done against buoyancy in entraining air could account for up to 50% of the energy lost from the wave field. Taken together, these results suggest that a detailed understanding of the energy balance in air-entraining breaking waves must account for the influence of the bubbles on the flow; but this would appear to be beyond our present experimental techniques.

It is interesting to compare these experimental findings with some recent numerical work by Chen, Kharif & Zaleski (1999). They simulated two-dimensional breaking, including splash-up and air entrainment following the impact of the jet on the surface ahead. They found that 80% of the pre-breaking wave energy was dissipated within three wave periods after breaking and that it subsequently decayed as t^{-1}, consistent with the measurements of RM. They found that much of the vorticity generation occurred during the period of jet impact, splash-up and air entrainment, although the details remain to be resolved. While consistent with RM, it must be remembered that these are two-dimensional simulations and cannot account for all aspects of the three-dimensionality of the real flows.

Duncan *et al.* (1994, 1999) have undertaken detailed studies of the fine-scale structure of the evolution of the crest profiles of very gently spilling waves. They find that in each case the beginning of the breaking process is marked by the formation of a bulge near the crest on the forward face of the wave, with capillary waves forming ahead of the bulge. At this stage, the profiles look quite similar to steady nonlinear gravity–capillary wave profiles computed by Fedorov & Melville (1998; see also Federov, Rozenberg & Melville 1999), which show an overhanging bulge preceded by capillary waves. However, it is clear from the experiments of Duncan *et al.* that these profiles rapidly lead to breaking, with the toe of the breaker proceeding down the forward face of the wave, while disturbances are swept back over the crest.

Lin & Rockwell (1995) measured quasi-steady breaking in a channel flow past a hydrofoil, pointing out that given the inherent unsteadiness of the flow, 'whole-field instantaneous technique(s) (are necessary to characterize) the velocity field at a given instant'. Using images of up to 64 mm in the horizontal dimension, they undertook careful particle image velocimetry (PIV) studies of the breaker at varying Froude numbers (based on flow speed and hydrofoil chord), finding that as the Froude number was increased the breaker evolved from a small-scale capillary pattern (similar to that described above), to a larger scale separated region. Both the capillary waves and the flow separation at the surface led to regions of concentrated vorticity, with circulations of the same order of magnitude.

Chang & Liu (1998, 1999) have measured turbulence under quasi-periodic breaking waves using PIV techniques. They generated a monochromatic wavetrain in shallow water and used ensemble-averaged statistics to characterize the mean flows and turbulence. They only considered the first few waves in the train to avoid reflection effects from the opposite end of the channel, and found that the mean transverse vorticity was of the same order of magnitude as C/h where C is the phase speed and h is the water depth. The maximum turbulence intensity outside the region aerated by bubbles was $O(0.1)C$. Examining contributions to the turbulent kinetic energy equation, they found that turbulence advection, production and dissipation were of comparable importance.

With the development of digital particle image velocimetry (DPIV) techniques that provide improved spatio-temporal coverage when compared to the point-by-point laser-Doppler velocimetry (LDV) measurements of RM, we considered it timely to return to a study of the unsteady breaking of individual waves. As RM showed, such breaking differs qualitatively from quasi-steady breaking since the region directly mixed down by the breaking is of finite extent in the direction of wave propagation. This contrasts with the infinite wake extending downstream from quasi-steady breaking waves. It also contrasts with quasi-periodic breaking in shallow water which may be a good model for depth-induced shoaling as waves approach the shore. The unsteady breaking studied by RM was generated by dispersive focusing of the waves, a process which undoubtedly occurs in both deep and intermediate-depth water.

In this paper, we use DPIV techniques to measure the velocity and vorticity fields under breaking waves in the laboratory. We use the dispersive focusing technique to generate intermediate or long packets of deep-water waves. Thus, the conditions of the experiments could correspond to the breaking of wind waves and swell on the continental shelf, where the depth is not directly important for the individual waves, but may be for the long waves forced by the modulation of the carrier waves. Despite the spatial coverage provided by imaging techniques such as DPIV, we found that we could not cover the full dynamic range and spatial extent of the flow in one image frame. While the desire to directly measure the smallest turbulent (Kolmogorov) scales would have required frame sizes of $O(1)$ cm, the desire to image the whole flow would have required frames of $O(1)$ m. We concluded that detailed studies at the Kolmogorov scales were premature before the overall kinematics of the flow were measured, and so we decided to conduct a series of measurements designed to characterize the larger coherent structures in the flow and look at the integral properties of the flow based on the energy bearing scales. Even with this decision it was not possible to image the whole flow with sufficient spatial resolution and we decided to build up a 'picture' of the whole flow with a 'mosaic' of individual frames. Since each realization of the flow is unique, such a scheme depends on our ability

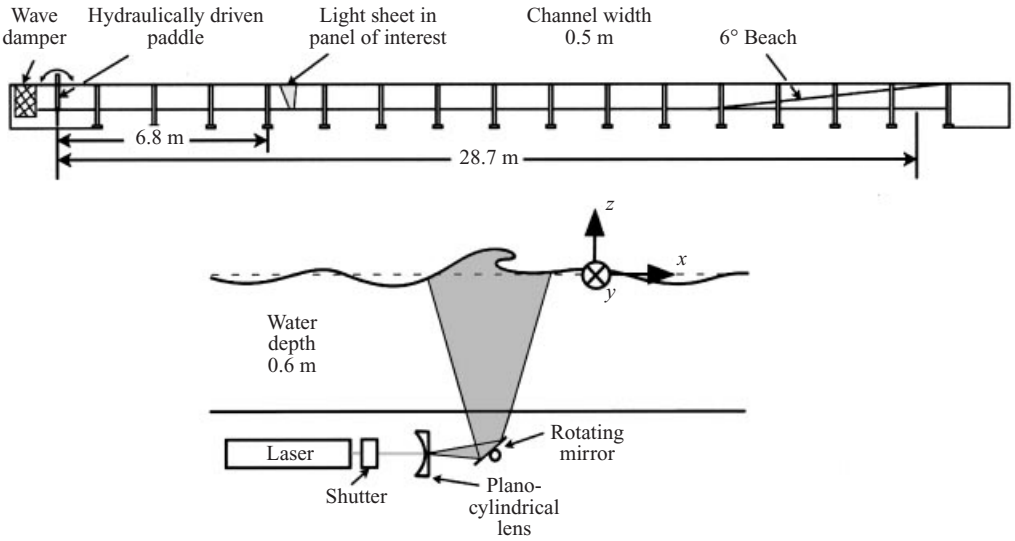

FIGURE 1. The glass wave channel at Scripps Institution of Oceanography and the detail for the DPIV light sheet.

to build up the coherent features of the flow and the statistics through ensemble averaging.

In § 2, we describe the experimental facility, the instrumentation and the methods used to create the overall flow from a mosaic of smaller frames. In § 3, we present the measurements of the mean and turbulent fields based on the coherent ensemble averaging. In § 4, we discuss the significance of these results in the context of related laboratory and field measurements. Estimates of turbulent dissipation from the DPIV data and comparable measurements using the acoustic techniques of Veron & Melville (1999) are presented in Appendix A. Estimates of the majority of terms in the turbulent kinetic energy balance are presented and discussed in Appendix B.

A preliminary version of this work was presented at the Air–Sea Interface Symposium, Sydney, January 1999 (Melville *et al.* 1999).

2. The experiments

2.1. *Breaking-wave generation*

The experiments were carried out in the glass wave channel in the Hydraulics Laboratory at Scripps Institution of Oceanography. The channel is 30 m long, 0.5 m wide and for these experiments the water depth was 0.6 m. At one end of the channel is a hydraulically actuated computer-controlled wavemaker; at the other, a beach covered with synthetic horsehair dissipates the waves (figure 1).

Breaking waves were generated at a distance of 7–9 m along the channel from the wavemaker by using the dispersive focusing method (RM) with a discrete spectrum of 32 wave components of constant slope ak about a central frequency $f_c = 0.99$ Hz, where a is the component amplitude and k its wavenumber (Loewen & Melville 1991). This differs slightly from RM who used a constant component amplitude. The resulting breaking was found to be extremely repeatable in both space and time to within 1 cm and $O(10^{-2})$ s, respectively. The centre frequency corresponds to a period

$T_c = 1.01$ s, a linear phase speed $C_c = 1.55\,\mathrm{ms}^{-1}$ and a wavelength $\lambda_c = 1.57$ m. The correction to the phase speed for finite depth effects is only 1%, so the individual waves are essentially deep-water waves while the wave group is long compared to the depth. For a given f_c and bandwidth, the governing parameter is the slope $S = 32\mathscr{G}ak$, where $\mathscr{G}$ is a gain parameter. Experiments were conducted for $S = 0.608, 0.656$ and 0.704, but most of the results presented here are for $S = 0.656$.

Surface displacement measurements were made with resistance wire wave gauges constructed of pairs of vertical nichrome wires of 0.015 cm diameter separated by 0.3 cm across the channel, feeding into Danish Hydraulic Institute electronics. The wave gauges, which were sampled at 50 Hz, were calibrated at the beginning and end of each day's experiments. Any d.c. drift from run to run during the day was subtracted using the first two seconds of (quiescent) data from each run.

2.2. *Digital particle imaging velocimetry: DPIV*

The equipment used for the DPIV is based on an early design of Willert & Gharib (1991), and a similar version using fibre optics was used by Melville, Shear & Veron (1998). A 5 W argon ion laser (American Laser Corp. Model 909) was used to generate a vertical sheet of light parallel to the sidewall of the channel. The beam from the laser passed through an electromechanical shutter (NM Laser products Model LS200FNC) which was controlled by a command signal from a timing circuit (General Pixels DPIV Timer 100) synchronized with the CCD camera (Texas Instruments TI1134P/GN: 768×480 pixels, 50 mm/f1.8 lens). The shutter and timing circuit were used to generate a flash of the laser sheet within each frame. After the shutter, the beam passed through a series of optical components terminating with a plano-cylindrical glass lens and a mirror that could be rotated to adjust the final position of the light sheet along the channel. The water in the channel was seeded with nearly neutrally buoyant Conduct-o-fil silver-coated hollow glass spheres (Potters Industries, Type SH400S33). Images were recorded on a Sony laser video recording system (LVR5000A, LVS5000A) which was connected by an RS232 communication line to the control computer. Images were later acquired by an EPIX 4MEG frame grabber card and stored on magneto-optical disk for later processing.

The basic image processing for the DPIV used software developed by Willert (1992) and Willert & Gharib (1991) which uses local (window) correlation techniques on image pairs to generate the velocity field. For this experiment, the time between consecutive frames was set to $\Delta t = 15$ ms for times less than 5 wave periods after breaking and $\Delta t = 51$ ms for later times. The technique requires that the images contain high particle densities since the processing correlates the grey scale of the images rather than the positions of individual particles. Given the Fourier transform relationship between the cross-spectral density function of image pairs and the cross-correlation function, much of the processing is done using forward and inverse FFTs.

One of the greatest challenges in applying DPIV to free-surface flows is the automatic detection of the interface, exacerbated by the fact that features that are local in the physical space are broadband in the Fourier space. To avoid masking by the meniscus on the near wall, for measurements containing the interface, the camera was angled upwards from beneath the lowest wave trough. This leads to three interfaces within an image: the far-wall interface, the intersection of the light sheet with the surface (the desired interface) and the near-wall interface. The far-wall interface was generally of low contrast and not a significant problem. The near-wall interface could be eliminated from the field of view by increasing the distance between the light sheet and the camera and therefore the vertical distance between the

light-sheet interface and the near-wall interface. Since the light-sheet interface tends to contain the brightest pixels in an image, a columnwise, iterative feature-searching technique, followed by horizontal median-smoothing was used to resolve the interface at the scale of one DPIV step size. Particles in the light sheet in the bulk of the fluid are reflected in the water surface between the light-sheet interface and the near-wall interface: mirror-image particles. It was found that the best way to eliminate this above-interface data, which is an artefact of the imaging, is to fill above the interface with a constant intensity value. This causes all displacements above the interface to be zero upon DPIV processing.

In order to increase the spatial resolution and accuracy of the determination of the velocity field, we used an iterative processing technique that we dubbed 'DPIV Extended' (DPIVE). A first processing of the data was made with an interrogation window of 32×32 pixels to give a low-resolution estimate of the velocity field. This was then refined by displacing smaller interrogation windows of 8×8 pixels by the distance corresponding to the first estimate of the velocity, before the standard correlation processing was repeated to give a corrected velocity estimate at the final resolution of $2.9 \times 2.9\,\mathrm{mm}^2$. Details may be found in White (1996).

Figure 2 shows an example of the results of this processing around the crest of a wave approaching breaking, acquired with a camera tracking the wave. (In all the other data presented in this paper, the camera was fixed in the laboratory frame as the waves propagated from left to right.) Figure 2(*a*) shows the raw image with the bright light–sheet interface. Near the crest, the bright region bifurcates with an artefact of bright light extending almost vertically as the true interface continues off to the left almost horizontally. We presume the vertical feature is associated with light 'leaking' into the crest region between the light–sheet interface and the near wall. Figure 2(*b*) shows the results of the processing to find the interface (bright dotted line) and setting the above-interface region to a constant intensity. Note that the region within half a DPIV interrogation window below the interface has also been set to the same constant intensity. This marks the proximity to the surface that can be achieved with the DPIV processing, which in this case is 1.5 mm. Figure 2(*c*) shows the final results of the interface and DPIV processing on the image in figure 2(*a*).

2.3. *DPIV mosaic and ensemble processing*

Following RM, we initially undertook dye studies to determine the region of the flow directly affected by the breaking. Prior to generating a breaking wave, dye was floated on the surface in the breaking region. At breaking, it mixed into the water column and continued to evolve with time. Figure 3 shows an example of dye clouds for three slope parameters at 20 s after breaking. It soon became clear that since the camera's field of view would only cover a small area of the breaking region, the flow in areas of this size could not be adequately resolved by single image pairs. Figure 3(*c*) shows the mosaic of 'tiles', or fields of view, that were used to reconstruct the whole flow. Since reproducibility of position and some level of automation were required to facilitate the data gathering, the camera's position on a horizontal track of linear bearings was under computer control with a stepper motor and belt drive. The vertical position of the tile was determined by tilting the camera in a vertical plane. Tiles were overlapped by a discrete number of DPIV interrogation windows so that overlapping vectors in adjacent tiles were aligned. Figure 3(*c*) shows the 3 rows and 8 columns that made up the mosaic for the strongest breakers.

The ability to reconstruct the coherent features of the flow and the turbulence statistics depends on the convergence of the means over a number of repeats of

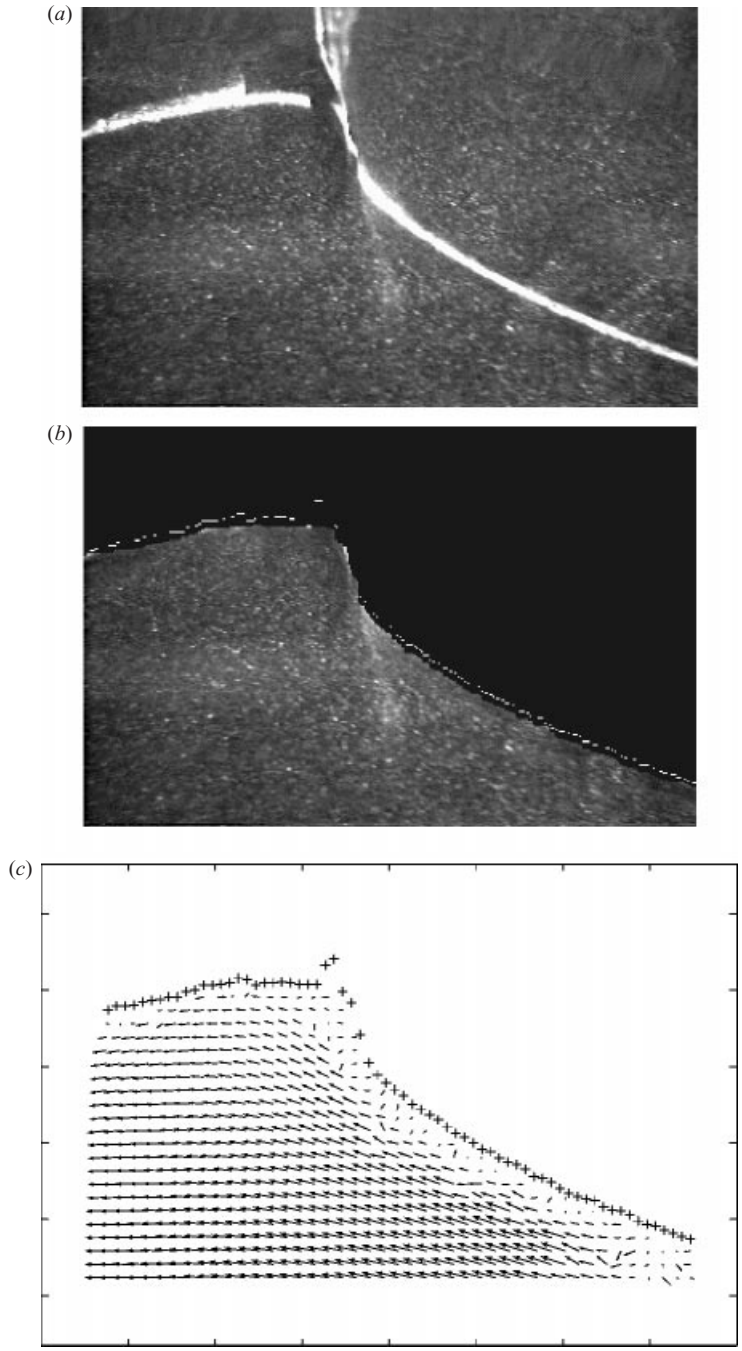

FIGURE 2. DPIV processing and interface detection. (*a*) An example of a raw video image showing the wave crest approaching breaking with particle reflections in the surface. (*b*) The above image processed to detect the interface and set the reflected area to a homogeneous intensity. (*c*) The velocity vector field computed for the images above.

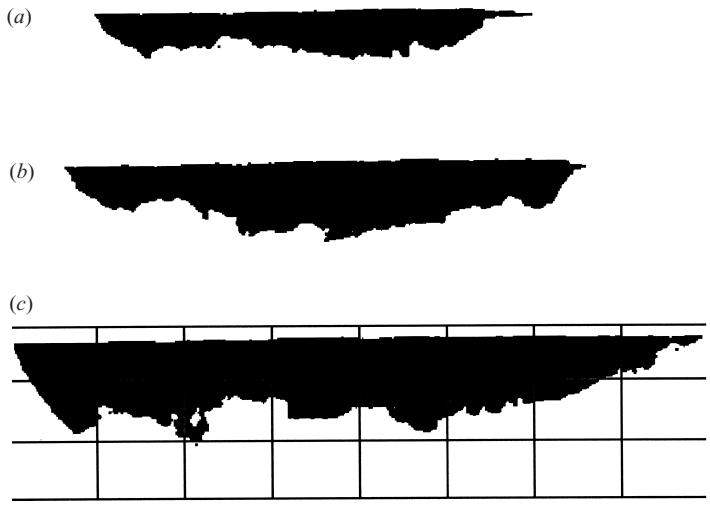

FIGURE 3. Dye-study images of the mixed region at 20 s after breaking for $S = 0.608, 0.656$ and 0.704, respectively. The image in (c) is superimposed on the grid of 24 video frames or tiles required to generate the composite DPIV results for the whole flow. Each tile is 21.6 cm long by 13.6 cm high.

the experiments. Any errors will show up along the boundaries of the tiles unless a sufficient number of samples are taken. The measured ensemble-average of the variable $\mathscr{P}(\boldsymbol{x}, t)$ is defined to be

$$P(x,t) \equiv \langle \mathscr{P}(\boldsymbol{x},t) \rangle_N \equiv \frac{1}{N} \sum_{i=1}^{N} \mathscr{P}(\boldsymbol{x},t)_i, \tag{2.1}$$

where the sum is over all realizations, N, of the flow. The measured turbulent component of the flow $p(\boldsymbol{x}, t)$ is then defined to be

$$p(\boldsymbol{x},t)_i = \mathscr{P}(\boldsymbol{x},t)_i - P(\boldsymbol{x},t). \tag{2.2}$$

The true ensemble average and turbulent component are just the limits of the above quantituies as $N \to \infty$. The error associated with the finite sum in the measured quantities can be estimated by conducting a large number of repeats of the experiment and evaluating the convergence as a function of N.

Convergence tests of the measured velocities were conducted on data acquired in the most energetic region of the breaking wave. This corresponds to the third column first row of figure 3(c). A total sample of 24 repeats was used for these tests. The normalized error in the squared magnitude of the mean velocity at the Nth realization, δU_N, is defined by

$$\delta U_N = \frac{\sum_{ij} |\boldsymbol{U}_N - \boldsymbol{U}_{24}|^2}{\sum_{ij} |\boldsymbol{U}_{24}|^2}, \tag{2.3}$$

where the sum is taken over all the $i \times j$ velocity vectors in the tile. The corresponding

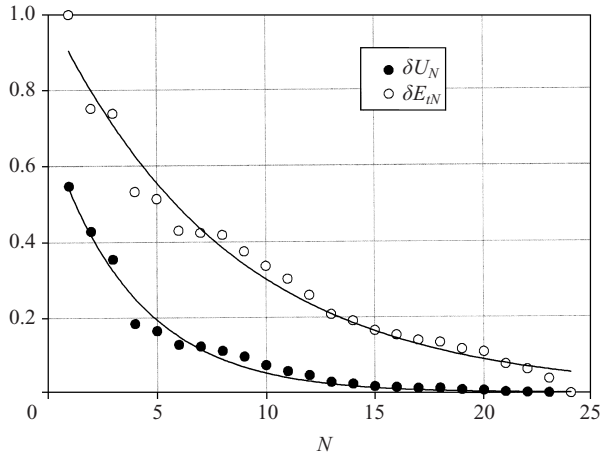

FIGURE 4. Examples of convergence of the normalized ensemble-averaged velocity magnitude, ●, and the corresponding normalized turbulent kinetic energy, ○, based on a total sample size of 24 repeats. The data shown in this paper were computed for production runs of 15 repeats, giving relative errors of approximately 2% and 16%, respectively.

error in the turbulent kinetic energy, δE_{tN} is given by

$$\delta E_{tN} = \frac{\sum_{ij} |E_{tN} - E_{t24}|}{\sum_{ij} E_{t24}}, \tag{2.4}$$

where E_{tN} is the estimate of the turbulent kinetic energy based on N repeats. Figure 4 shows that for production runs of 15 repeats, the normalized error in the mean velocity is approximately 2% and that in the turbulent kinetic energy approximately 16%, when referred to an ensemble of 24 repeats.

3. Results

Unless otherwise indicated, all length, time and velocity scales are normalized by the characteristic wavelength, λ_c, period, T_c, and phase speed, C_c, respectively. (The vorticity is normalized by the radian frequency $\omega_c = 2\pi/T_c$.) Times and horizontal distance used to described the data are relative to the break point (t_b, x_b) defined to be the position in time–space at which the wave impacts on the water surface ahead. All ensemble averages are computed over 15 repeats of the experiment.

3.1. *Mean velocities and vorticity*

Figure 5 shows the evolution of the mean velocity $\boldsymbol{U}(\boldsymbol{x}, t)$ from 3 to 58 wave periods after breaking constructed from a mosaic of frames, or tiles, of 21.6 cm × 13.6 cm, starting at $x = 0.13$. (Note that all subsequent figures showing ensemble-averaged fields in (x, z) are for the same times as in figure 5.) The first panel shows that surface waves, with significant regions of convergence and divergence of the horizontal velocity in the horizontal direction, and significant vertical velocities near the surface, are still propagating out of the measuring region to the right. By the second panel, $t = 10.5$, there is still some sign of the orbital velocity components at $x = 0.4$, but, a mean vortex centred about $x = 0.6$ is already apparent. As time proceeds, this feature,

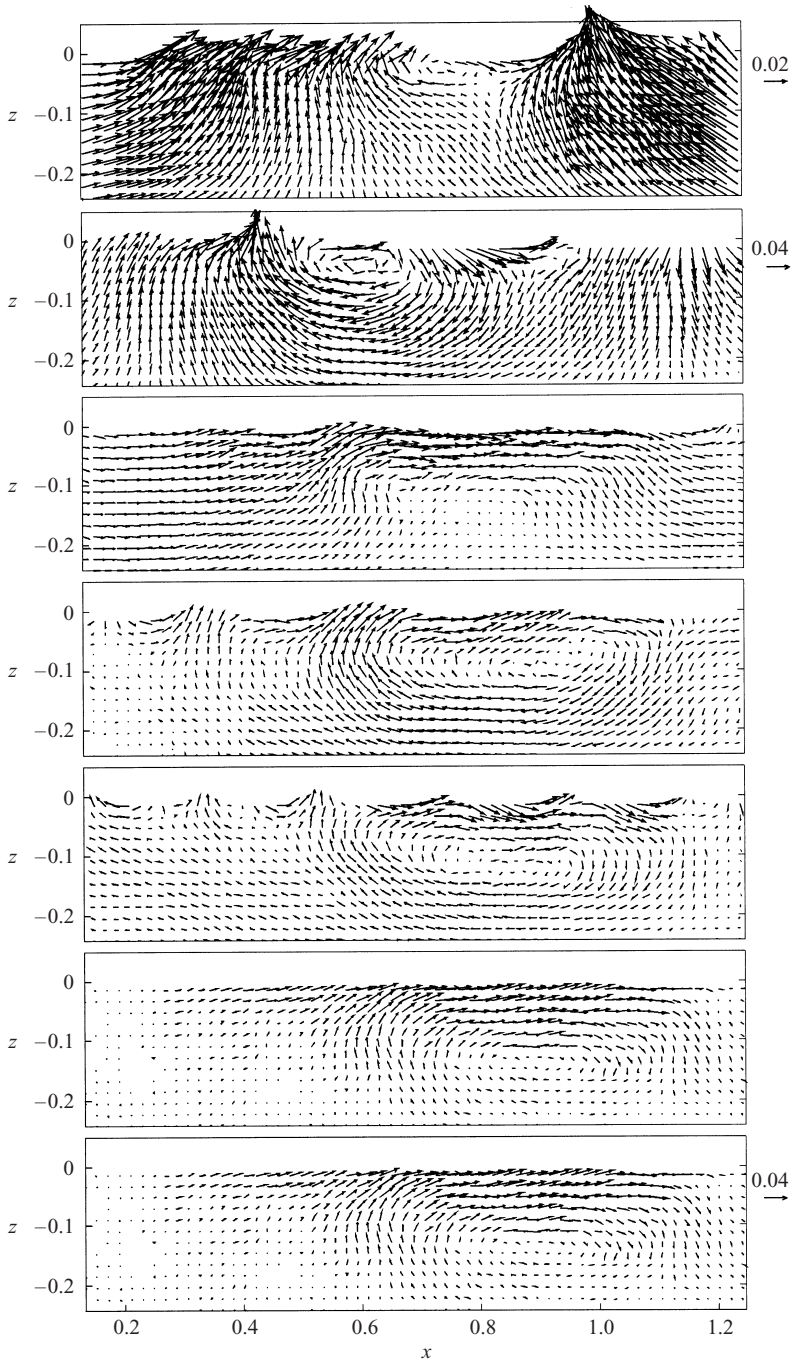

FIGURE 5. The mean velocity field at times $t = 3$, 10.5, 26.5, 34.5, 42.5, 50 and 58 for $S = 0.656$. For convenience in constructing the figure, the data points are decimated by a factor of 10 in each direction. The top panel shows large orbital velocities as the waves propagate across the measurement region to the right. Subsequently, the main feature that distinguishes the mean velocity is a coherent vortex slowly propagating to the right. Note the different scale for the first panel.

which will be described in more detail below, slowly propagates to the right, so that at $t = 58$ it is centred about $x = 0.95$.

Using the undecimated data represented in figure 5, we have shown in figure 6 the streamlines of the mean flow along with a colour-coded display of the velocity magnitude. The streamline patterns, especially in the last four panels, are consistent with a coherent vortex of positive vorticity (clockwise circulation) propagating downstream and deepening.

The mean vorticity is computed as the local circulation of the mean velocity field on a 5×5 grid, divided by the included area. Figure 7 shows the evolution of the mean vorticity field over the same time interval as figure 5. With the exception of a very thin region at the surface where the vorticity is negative, the mean vorticity is predominantly positive corresponding to a clockwise circulation in the plane of the page. In laboratory measurements and numerical simulations, Chang & Liu (1999) and Lin & Liu (1999) have found thin surface regions of negative vorticity consistent with surface sources of vorticity near the break point. Given the important role of the rising bubbles in generating vorticity, it is not clear that a thin vortical layer near the surface would remain intact until the later times of our measurements. Our measurements are not of sufficient resolution to be definitive on the source of the thin layer of negative vorticity and the possibility that it is an artefact of the near-surface processing must be acknowledged. Note that the effects of the waves, which were apparent in the first few frames of the velocity field, have been effectively filtered out by taking the curl of the velocity. That is, the waves are, to a good approximation, irrotational. The magnitude of the mean vorticity decreases from a maximum of 0.5 at $t = 3$, to 0.04 at $t = 58$, while it extends from a depth of $z = 0.02$ to 0.05 over the same period.

Using incompressibility and computing the divergence of the mean flow in the vertical plane confirmed that $\partial V/\partial y$, the lateral gradient of the mean flow was negligible and therefore to a good approximation the mean flow was two-dimensional.

3.2. *Kinetic energy*

The two-dimensional mean kinetic energy density E is defined to be

$$E = \tfrac{1}{2}\langle (U_i + u_i)^2 \rangle, \tag{3.1}$$

$$= \tfrac{1}{2}(U_i^2 + \langle u_i^2 \rangle), \tag{3.2}$$

$$= E_m + E_t, \tag{3.3}$$

where E_m and E_t are the kinetic energy density of the mean and turbulent flows, respectively, and the summation of i is over the two measured components of the velocity.

Figure 8 shows the evolution of E_m. As might be expected from figure 5, the first time shown is dominated by the kinetic energy associated with the waves propagating across the measurement region. These panels also show some evidence of the vertical boundaries of the tiles used to construct this mosaic. Given the large dynamic range associated with the combination of waves and turbulence, it is difficult to find a colour scale that also adequately represents the later stages of the evolution of E_m, but even so, it is clear that the kinetic energy of the mean flow is also associated with the vortex propagating downstream.

The turbulent kinetic energy density is shown in figure 9. Now the effect of the coherent waves has been averaged out and the kinetic energy associated with the incoherent turbulence emerges, especially in the first panel. This panel also shows

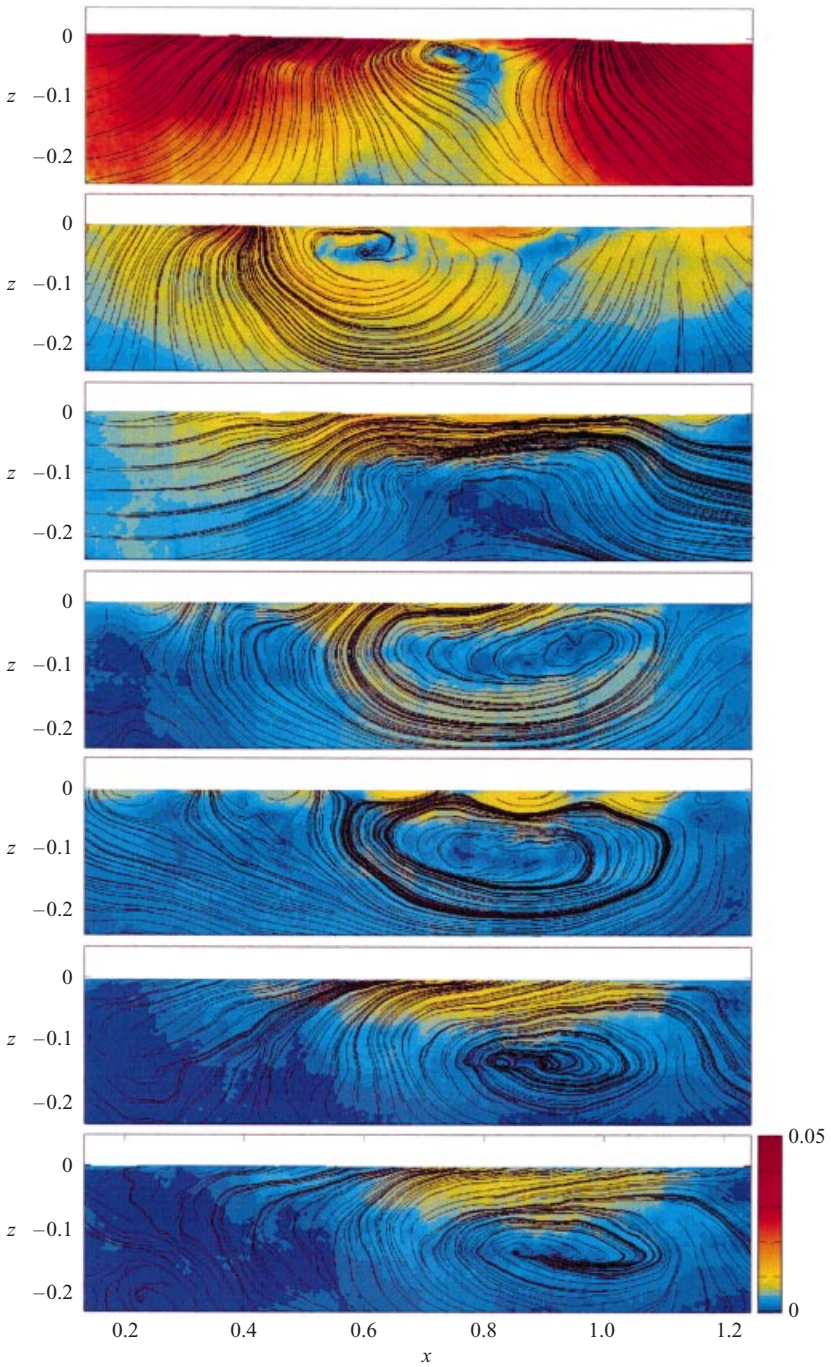

FIGURE 6. The streamlines corresponding to the mean flow shown in figure 5. The colour code shows the magnitude of the mean velocity. As shown in figure 5, the main feature is a coherent vortex which slowly propagates downstream and deepens.

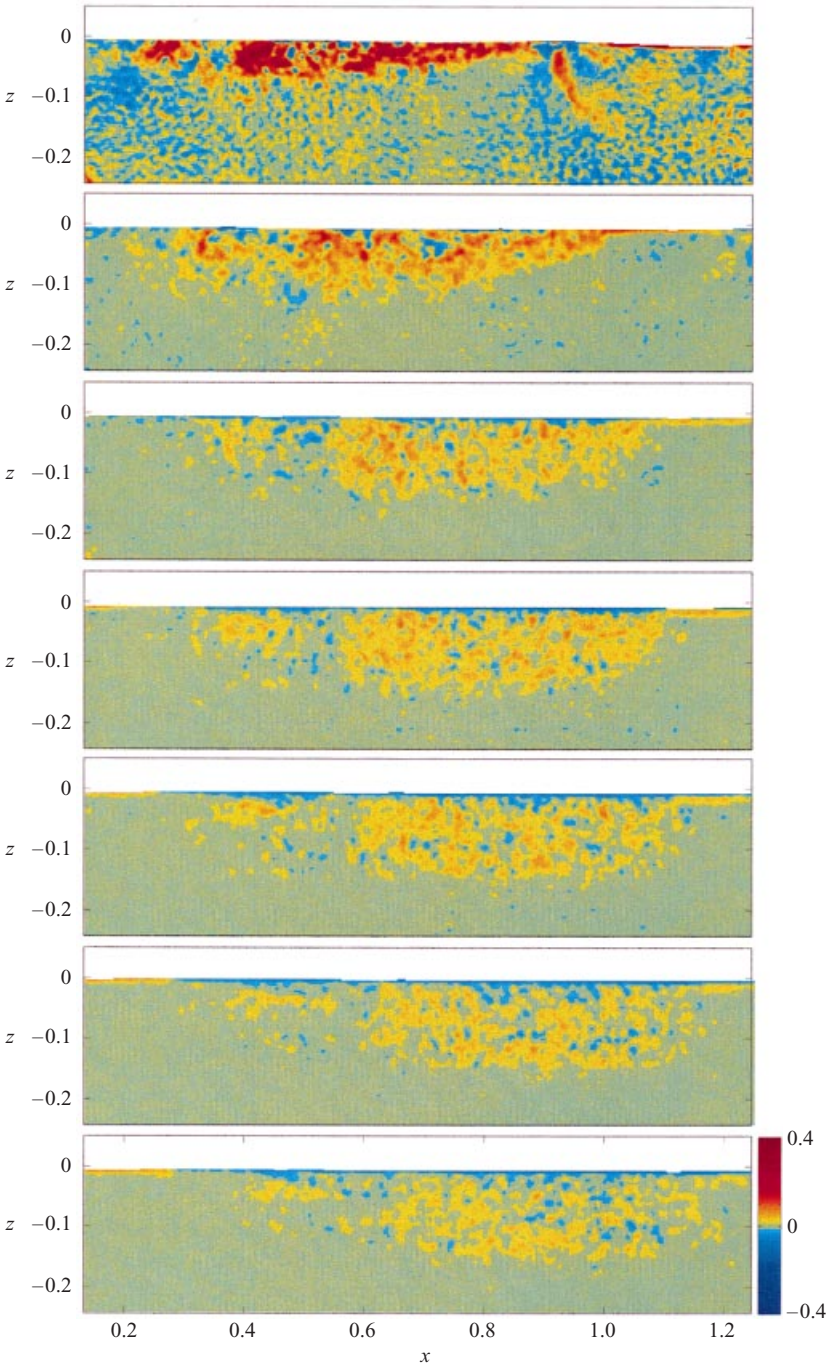

FIGURE 7. The vorticity of the mean flow. Note the slow advection downstream and deepening of the region of positive vorticity as time increases.

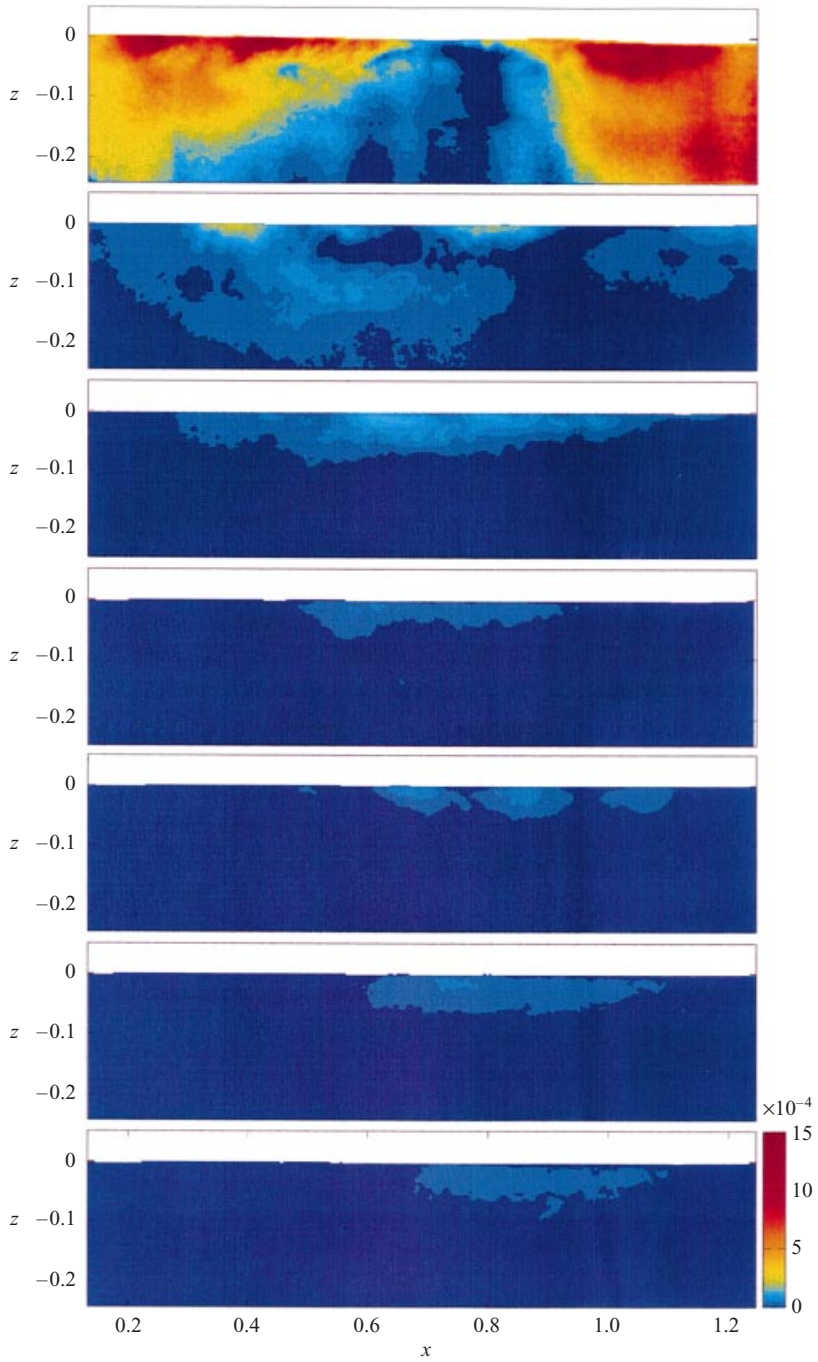

FIGURE 8. The kinetic energy density of the mean flow. Note the large levels of kinetic energy in the first frame which correspond to the contribution from the orbital velocities of the waves still in the measuring region. At later times, the kinetic energy is advected slowly downstream, cf. figure 5.

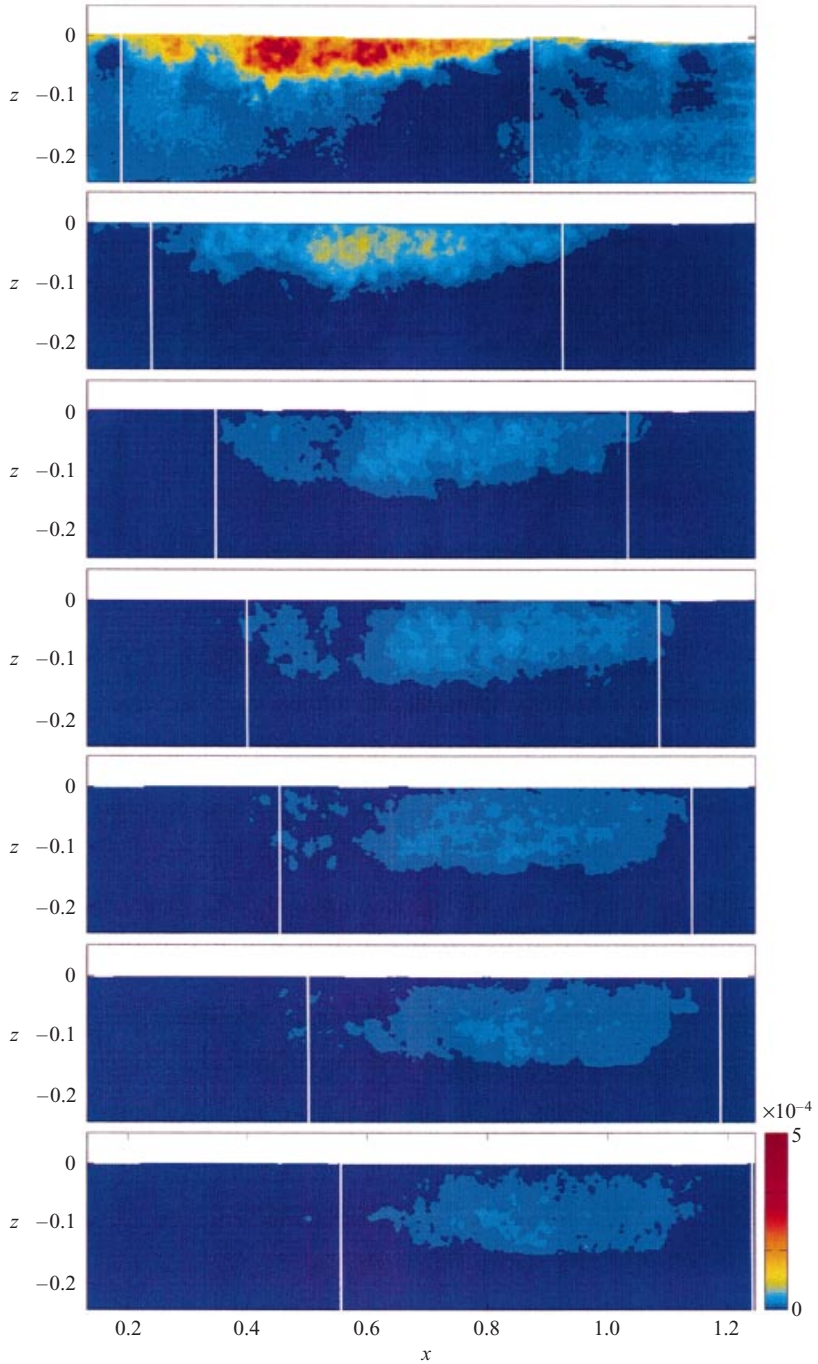

FIGURE 9. The turbulent kinetic energy density, E_t. The high levels of turbulence initially generated by the breaking are clearly evident at the first few times. Also evident are the vertical boundaries of the DPIV tiles. The region of high E_t slowly advects downstream while deepening. The vertical lines represent the position the breaking induced vortex would be when propagating at a speed of $0.012\,\mathrm{m\,s^{-1}}$. These lines are also used to horizontally bound certain averages in the data processing.

some small residual errors due to the mosaic, but they are well below the maximum energy densities. The patch of E_t at $t = 3$ extends over a depth of approximately 0.08 and along the channel for approximately $0.8\lambda_c$. By $t = 58$, it has mixed down to $z = 0.15$, but the dispersion along the tank is negligible. This is consistent with the dye mixing studies of RM who showed that following a rapid increase of the front of the mixed region for a time of order one wave period, the subsequent length of the dye cloud increased only very slowly, if at all.

3.3. *Vorticity*

The mean square vorticity $\mathscr{V}$ (or twice the enstrophy) is defined by

$$\mathscr{V} = \langle(\Omega + \omega)^2\rangle, \tag{3.4}$$

$$= \Omega^2 + \langle\omega^2\rangle, \tag{3.5}$$

$$= \mathscr{V}_m + \mathscr{V}_t, \tag{3.6}$$

where, Ω is the mean vorticity, $\mathscr{V}_m$ is the square of the mean vorticity and $\mathscr{V}_t$ is the mean-square turbulent vorticity.

Figure 7 shows the mean vorticity, which, with the exception of the negative surface values discussed, is positive throughout the volume of fluid mixed down by the breaking. That is, it is consistent with a flow in the direction of wave propagation near the surface with a return flow below, as shown in figure 5. The persistence of this feature has implications for both the turbulent kinetic energy balance near the surface and the fine-scale structure of the surface, both of which will be discussed below.

It is well known that while the turbulent kinetic energy resides in the larger scales of turbulence, the vorticity of the turbulence is associated with the smaller dissipative scales. Based on the data in figure 13 and estimates of dissipation for the same flow in Veron & Melville (1999), we estimate the Kolmogorov microscale $\eta = (\nu^3/\epsilon)^{-1/4}$ to be $O(1)$ mm, or a little larger in the spatio-temporal regions of the flow shown here. However, with the vorticity computed by the circulation around squares of $6 \times 6\,\mathrm{mm}^2$, we are not resolving the full turbulent vorticity field; however, it is still worth recording the measurements. Figure 10 shows the mean square vorticity of the larger eddies. Again, as expected, the turbulent vorticity is transported downstream with the mean eddy, and to depth by both advection and turbulent transport.

Using incompressibility and computing the divergence of the turbulent field the vertical plane, it may be shown that $\partial v/\partial y$ is comparable to the turbulent strain rates in the vertical plane.

3.4. *Reynolds stress*

The Reynolds stresses are important for transferring horizontal momentum vertically into the water column. In figure 11, we show the turbulent Reynolds stress $\langle uw\rangle$ as the flow evolves. Note that while noisy at the larger times, the Reynolds stress is consistently negative, indicating that positive horizontal momentum is being transported vertically downwards. This is discussed at some length in § 4.

3.5. *Temporal evolution*

The fields from figures 7 to 10 are areally integrated over the panels of those figures to give integral measures of kinetic energy and mean square vorticity as a function of time in figure 12. At the first two times, the kinetic energy is elevated by the waves remaining in the measuring region, but the total kinetic energy subsequently represents that

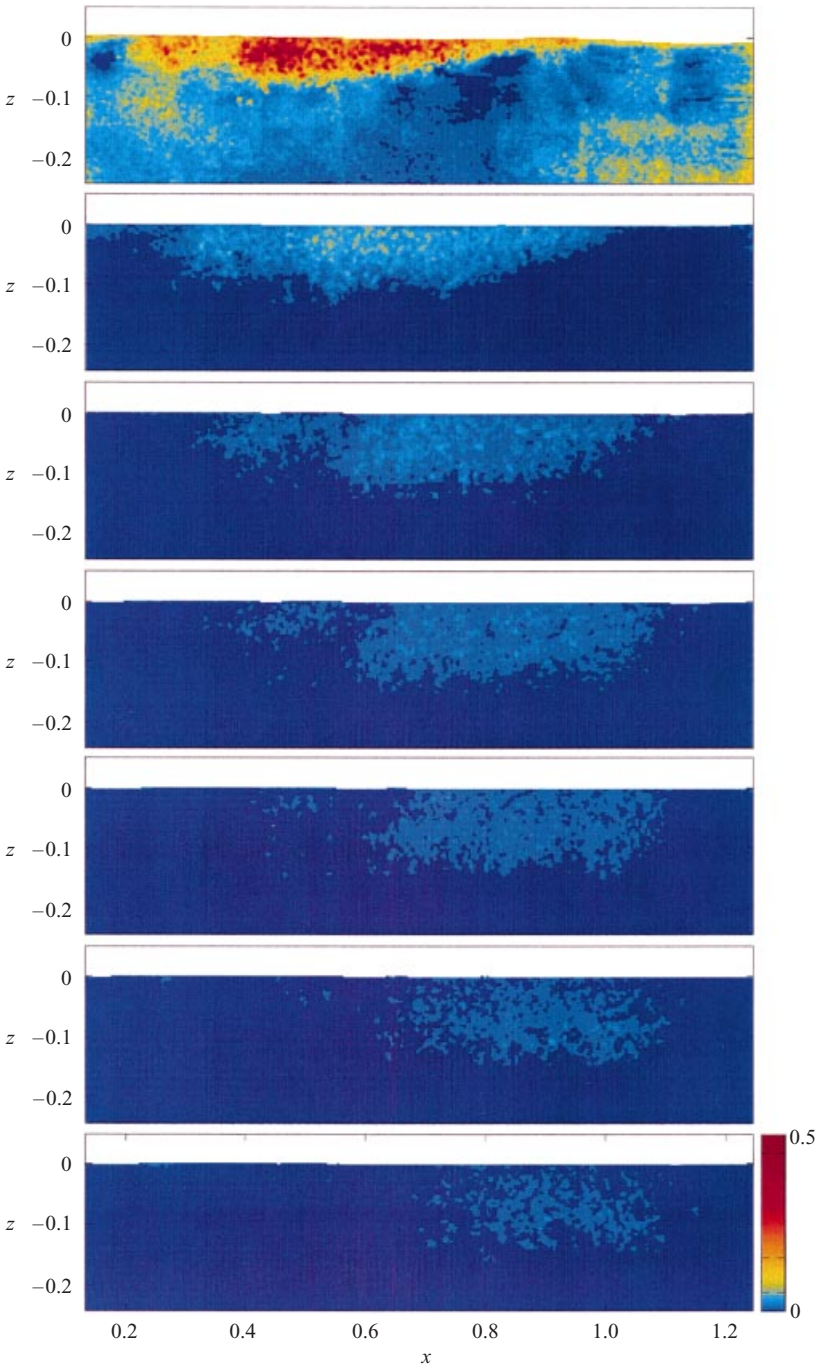

FIGURE 10. The mean square vorticity of the turbulence $\mathscr{V}_t$. As expected, this is significant over the same region of the flow as the turbulent kinetic energy, E_t.

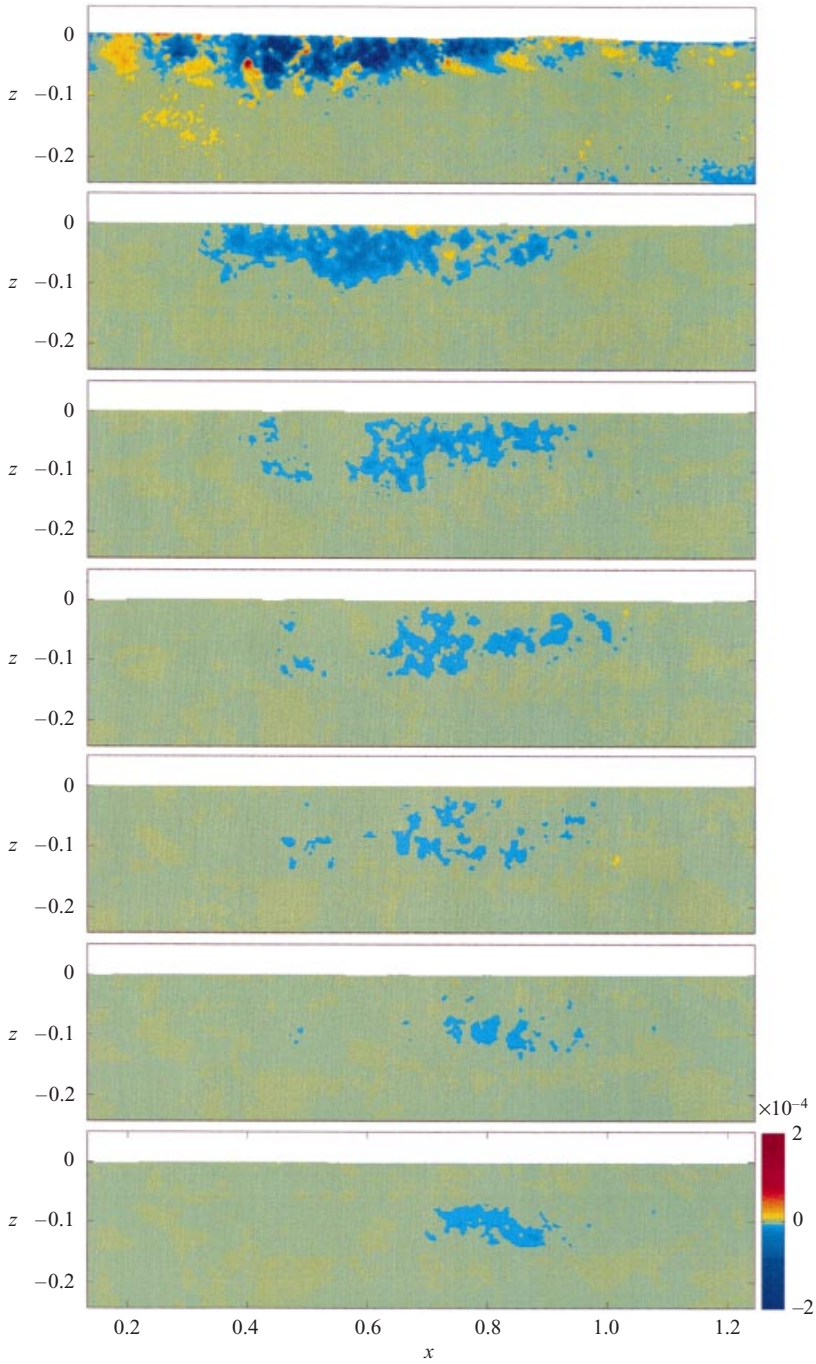

FIGURE 11. The turbulent Reynolds stress. Note that this stress is predominantly negative, corresponding to the downward transport of positive horizontal momentum.

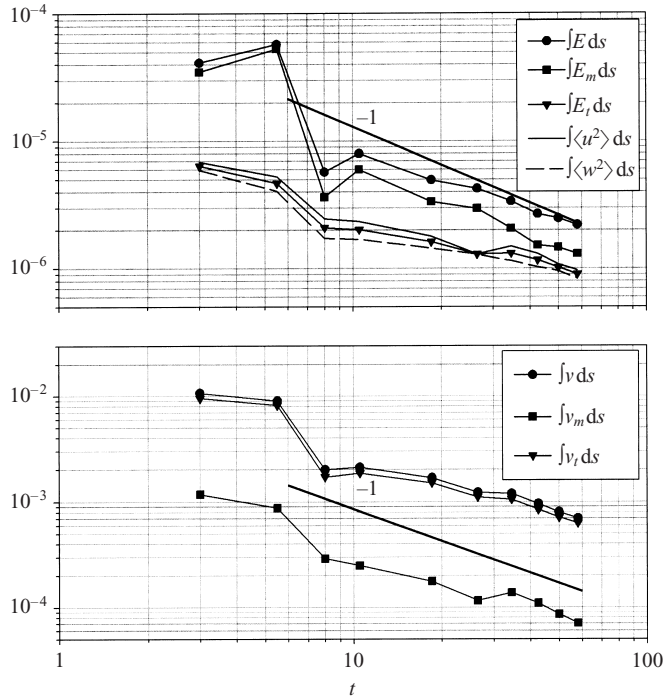

FIGURE 12. Evolution of the areal integrals of kinetic energy and mean square vorticity with time. Note the decrease in kinetic energy of the mean flow between $t = 5$ and $t = 8$, as residual waves propagate out of the measuring region.

resulting from the breaking and this quickly decays approximately as t^{-1}, consistent with RM's results. Throughout the duration of the measurements, the kinetic energy of the mean flow, E_m, is larger than that of the turbulence, E_t, but the slopes of the lines are consistent with a transfer of energy from the mean flow to the turbulence (see below). In contrast (figure 12*b*), the mean square turbulent vorticity is consistently larger than the square of the mean vorticity, but again both decay approximately as t^{-1}.

Figure 13 shows horizontal averages (vertical profiles) of the turbulent kinetic energy, mean square turbulent vorticity and the Reynolds stress as a function of time. It is clear from all of these profiles that the maxima are not at the surface, but coincide with the depth of the core of the mean vortex generated by the breaking. This deepens from $z \approx 0.02$ to 0.07 over the time covered by these experiments.

3.6. *The drifting eddy*

The dominant feature of the post-breaking velocity field is the coherent eddy that drifts slowly downstream at the same speed as the patch of smaller-scale turbulence. Using correlation techniques based on the data in figure 9, over times $t = [3, 58]$ the mean downstream speed of the eddy is $0.012\,\mathrm{m\,s^{-1}}$. Figure 14 shows the circulation as a function of time and of the area of the enclosed circuit for circuits extending along the surface horizontally for a distance of 0.7, and then returning horizontally at depth, with different depths giving different areas. The circuits move downstream at the advection velocity of the vorticity (see figure 9). Since the circulation tends to a constant value for each time (but decreases with time), it implies that there is a rotational core surrounded by effectively irrotational fluid. We wish to determine whether the downstream drift of the eddy can be accounted for by the induced

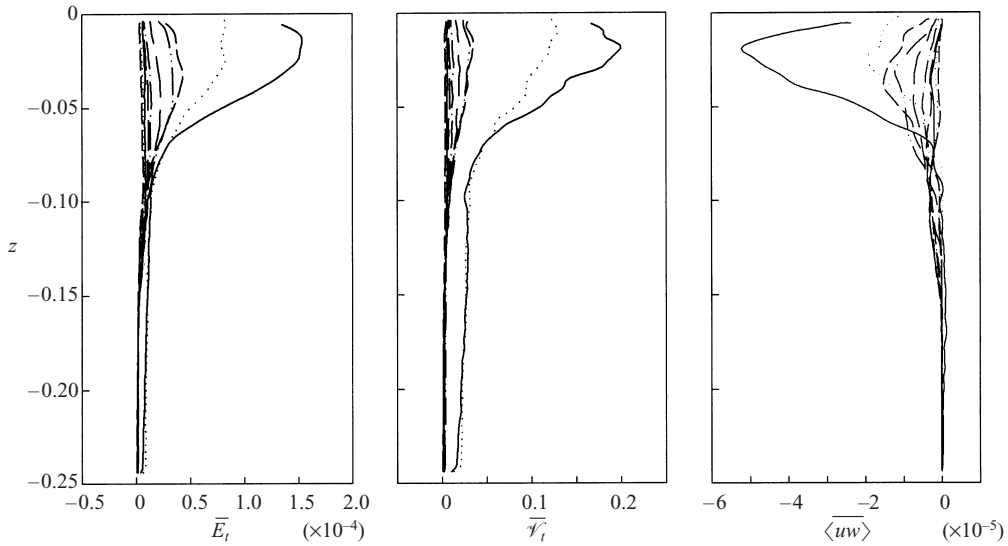

FIGURE 13. Averaged horizontal profiles of the mean turbulent kinetic energy, $\overline{E}_t$, the mean square turbulent vorticity, $\overline{\mathscr{V}_t}$, and the Reynolds stress, $\overline{\langle uw \rangle}$. Note that the horizontal average is over a length of 0.7 defined by the vertical lines in figure 9 which move at the speed of the turbulent cloud.

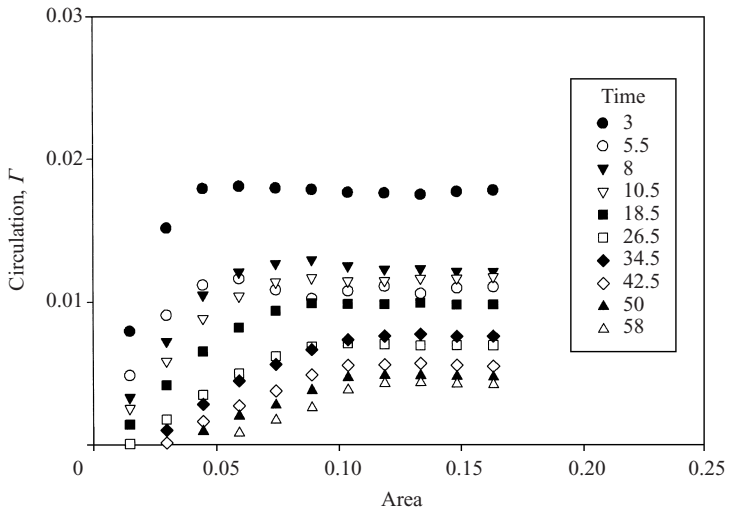

FIGURE 14. The circulation about clockwise rectangular circuits whose lateral boundaries are defined by the vertical lines in figure 9, the surface, and horizontal lines at different depths giving different enclosed areas. Note that the circulation tends to approximately constant values for enclosed areas greater than approximately 0.1.

velocity from the image vortex above the surface. A line vortex having a circulation Γ at a depth d below the surface will have an induced horizontal velocity of $\Gamma/4\pi d$. Taking the average circulation of $\Gamma = 0.0076$ over the times $t = [8, 58]$ and the core of the vortex at a depth of $d = 0.068$ (figure 7), we obtain a drift velocity of $0.0138\,\mathrm{m\,s^{-1}}$ which compares favourably with the measured velocity of $0.012\,\mathrm{m\,s^{-1}}$.

4. Implications for the field

While these are laboratory measurements under conditions in which the waves are deep-water but the wave groups are intermediate or shallow-water, we saw no evidence that the vertical mixing and evolution of the turbulence was inhibited by the presence of the bottom of the channel. Therefore, we believe that the data also have application to the evolution of turbulence under breaking waves in deeper water. While we have only presented detailed data for one particular set of conditions, experiments were conducted for different characteristic slopes with similar results. Of particular interest is the applicability of these results to the field. In this regard, two applications are significant.

4.1. *Wave breaking momentum flux*

First, the measurement of the Reynolds stress under breaking waves is novel and is of particular significance for field applications. It was shown by RM that the post-breaking velocity field satisfies Froude scaling so that when normalized by the pre-breaking wave scales, the velocity field is a function of the characteristic wave slope ak, and if viscous effects are significant, the Reynolds number, $R = C_c\lambda_c/\nu$, also. For the experiments described here $R = 2.43 \times 10^6$, sufficiently large that we expect that the turbulence fields will be asymptotically independent of R. For the detailed results presented here, $S = 0.656$, corresponding to moderate breaking strength, which is probably representative of breaking in the ocean. If this is the case, then the non-dimensional turbulent kinetic energy and Reynolds stresses may be considered representative of oceanic conditions.

We consider the contribution of breaking to the vertical flux of horizontal momentum. Following Phillips (1985), we define a distribution $\Lambda(c)$ such that $\Lambda(c)\,\mathrm{d}c$ represents the average total length per unit surface area of breaking fronts that have velocities in the range c to $c+\mathrm{d}c$. (In this section, for reasons of clarity of comparison with the literature we will use dimensional variables.) Now RM showed (see also Lamarre & Melville 1991; Loewen & Melville 1991; Melville 1994) that the duration of the active breaking at the surface, the time, τ_b, over which the 'whitecap' is extending in length, was approximately the characteristic wave period, T_c. However, the time period for decay of the turbulence, τ_t, the time over which the surface fluid and turbulent kinetic energy is mixed down can be significantly longer. Also, the visible persistence of the whitecap depends on the turbulence maintaining bubbles in the water column against their buoyant rise velocity. In fresh water, Lamarre & Melville (1991) showed that most of the entrained air (contained in the larger bubbles) rose back through the surface over a time of $O(T_c)$ and we expect that to be the case for salt water too. However, the visible persistence of the whitecap, especially in salt water, may be much longer, since rather small void fractions at the surface, $O(10^{-4})$ may lead to reflectances greater than those of seawater (Terrill, Melville & Stramski 1998, 2001). Differences in the surface electro-chemistry lead to larger concentrations of small bubbles in salt water; however, small bubbles do not contribute to significant void fractions. Phillips (1985, p. 529) used the persistence time of the bubbles to define the whitecap coverage. We believe that τ_b, the shorter time of active breaking, is the more appropriate time scale.

Over a short time τ_b, breaking imparts horizontal momentum to the near-surface layer. Over a longer time, the time scale for the decay of the turbulence, τ_t, momentum is transported vertically by the turbulent Reynolds stresses. In a random sea, it is most unlikely that the ensemble-averaged mean velocity that we can measure in the laboratory could be separated from the incoherent turbulence, so in the field both

would be considered to be 'turbulence'. The mean eddy that is formed does lead to a vertical transport of horizontal momentum, but for times at which we can make measurements (after the larger bubbles have degassed) it is small when compared with the turbulent transport. Now the area per unit area of surface swept out by breaking fronts in the speed range c to $c + \mathrm{d}c$ is $\tau_b c \Lambda(c)\,\mathrm{d}c$. The vertical flux of horizontal momentum averaged horizontally over the whitecap is $\rho_w \overline{uw}(t)$, where the horizontal average is denoted by the overbar. The total momentum transported vertically per unit area of whitecap, M, is

$$M = \int_0^{\tau_t} \rho_w \overline{uw}\,\mathrm{d}t, \tag{4.1}$$

$$= \tau_t \rho_w [\overline{uw}], \tag{4.2}$$

where the square brackets denote a time average over τ_t.

Thus, the distribution of breaking momentum flux with respect to wave speed, estimated from the vertical transport of horizontal momentum, is

$$I(c)\,\mathrm{d}c = \frac{\tau_t}{\tau_b} \rho_w [\overline{uw}] \tau_b c \Lambda(c)\,\mathrm{d}c, \tag{4.3}$$

where the τ_b in the denominator results from the fact that this momentum is initially transferred from waves to currents over the duration of active breaking, whereas its vertical transport by turbulence takes a significantly longer time, τ_t.

Consistent with RM and Loewen & Melville (1991), the duration of breaking, τ_b, is approximately one wave period, and the speed of advance of the breaking region is approximately $0.8C_c$, where C_c is the characteristic phase speed of the breaking wave. Therefore, using the linear dispersion relationship for deep-water waves, we have that $\tau_b \approx 2\pi C/g$, $\tau_t = \mathscr{T}\tau_b$ and $c = 0.8C$, where we have dropped the subscript on C, and $\mathscr{T}$ is a numerical factor. It follows that

$$I(c)\,\mathrm{d}c \approx \tau_t \frac{\rho_w [\overline{uw}]}{c^2} c^3 \Lambda(c)\,\mathrm{d}c, \tag{4.4}$$

$$= \mathscr{T} \frac{2\pi}{(0.8)^3 g} \frac{\rho_w [\overline{uw}]}{C^2} c^4 \Lambda(c)\,\mathrm{d}c. \tag{4.5}$$

We can estimate $[\overline{uw}]/C^2$, from the data of figure 13 using the values of $\overline{uw}$ from the depth of the maximum at $t = 3$ ($z = 0.02$) and integrating in time for fixed z. We find that the vertical transport of momentum at this level is essentially complete at $t = 50$, giving a value of $[\overline{uw}]/C^2$ of 1.4×10^{-5} and $\mathscr{T} = 50$. Thus, equation (4.5) becomes

$$I(c)\,\mathrm{d}c \approx 7 \times 10^{-3} \rho_w g^{-1} c^4 \Lambda(c)\,\mathrm{d}c. \tag{4.6}$$

To within a value of the numerical factor, this is the same as equation 3 of Phillips, Posner & Hansen (1999). Now, on the basis of integral constraints on the momentum flux across the air–sea interface and extimates of $\Lambda(c)\,\mathrm{d}c$, based on field measurements of radar backscatter from breaking waves, Phillips, Posner & Hansen (2001) concluded that the numerical factor in equation (4.6), b say, should be in the approximate range $[2, 5] \times 10^{-4}$, whereas based on the laboratory measurements of unsteady breaking by RM and Loewen & Melville (1991), Melville (1994) had b in the range $[3, 16] \times 10^{-3}$ and Duncan's (1981, 1983) measurements of quasi-steady breaking have b in the range $[3, 7] \times 10^{-2}$. While this independent estimate of b from these experiments is consistent with our earlier work, the differences between the estimates of what is effectively the dissipation rate of breaking waves, from quasi-steady and unsteady

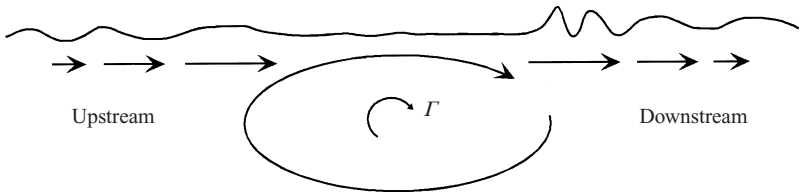

FIGURE 15. Definition sketch for short waves riding on the eddy generated by a breaking wave propagating to the right. Waves propagating downstream (to the right) do so on an accelerating current while those propagating upstream (to the left) do so against a decelerating current. For simplicity, we assume the eddy is stationary and the surface velocity tends to zero far upstream and downstream.

breaking experiments in the laboratory, and inferred values from field observations, need to be resolved.

4.2. *Breaking suppression of short surface waves*

Casual observation of breaking seas suggests that a broken wave leaves a 'scar' on the surface, which takes some time to reestablish the spectrum of shorter waves. Certainly the longer waves pass through the broken region, but shorter waves seem to be excluded. These laboratory measurements provide a plausible explanation for this phenomenon.

Figure 5 and the earlier work of RM (figures 42–45) show that the coherent eddy remains after breaking with velocities at the surface of $O(10^{-2}$–$10^{-1})C$ decaying to $O(10^{-2})C$ over approximately 50 wave periods. This eddy drifts slowly downstream at a speed of approximately $0.01C$ (figure 7). For simplicity, consider a stationary eddy and neglect all but the shorter waves that may propagate towards the broken region from either upstream or downstream. To retain the essential physics while neglecting complicating factors, we assume that the short wave field is steady in a frame of reference fixed on the eddy. This situation is represented in figure 15. From the figure, it becomes apparent that waves propagating downstream/upstream towards the eddy will encounter an accelerating/decelerating surface current. Geometrical optics and action conservation (Mei 1983, pp. 105–108) show that the waves propagating downstream will lengthen and decrease in slope while those propagating upstream will shorten and steepen, and, if the adverse current is sufficiently large, be blocked. The consequence of this wave–current interaction is that the broken region may be a region with short waves of lesser slopes.

Following Mei (1983) and designating reference values by $(\,)_o$ we obtain

$$\omega = kU + \sigma = k_o U_o + \sigma_o = \text{const}, \tag{4.7}$$

where k is the wavenumber, U the horizontal velocity at the surface, ω the radian frequency, and σ the intrinsic frequency. We assume that the scale over which there are vertical gradients of U is large compared to k^{-1}. Assuming that the short waves are long enough to be gravity waves, the phase speed c relative to the current is just $(g/k)^{1/2}$. For simplicity, we set the reference current far upstream and downstream $U_o = 0$. It follows that

$$\frac{k}{k_o} = 1 \Big/ \left(\frac{U}{c_o} + \frac{c}{c_o}\right), \tag{4.8}$$

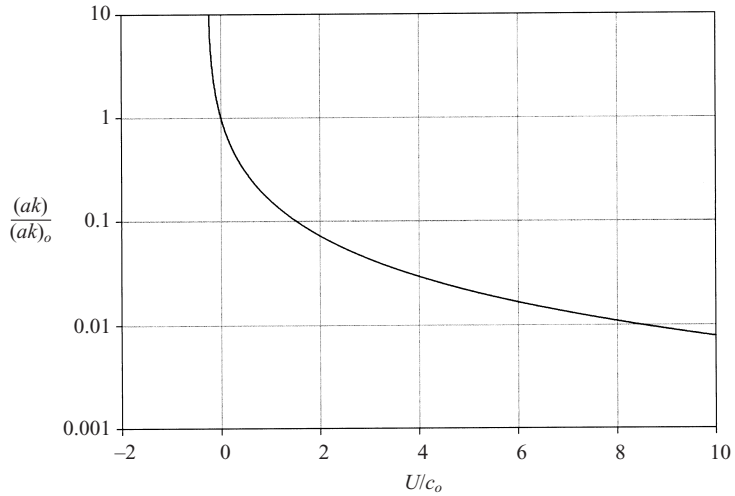

FIGURE 16. Normalized slope $(ak)/(ak)_o$ *vs.* U/c_o for gravity waves on a steady stream of counter- and co-flowing currents. Blockage may occur for small counter-flowing currents while a reduction in slope occurs for co-flowing currents (cf. figure 15).

$$\frac{a^2}{a_o^2} = \frac{c_o}{c}\frac{1}{c/c_o + 2U/c_o}, \tag{4.9}$$

whence

$$\frac{(ak)}{(ak)_o} = \left[\frac{c_o}{c}\frac{1}{c/c_o + 2U/c_o}\right]^{1/2} \Big/ \left(\frac{U}{c_o} + \frac{c}{c_o}\right), \tag{4.10}$$

and c/c_o can be eliminated by using

$$\frac{c}{c_o} = \frac{1}{2}\left[1 + \left(1 + 4\frac{U}{c_o}\right)^{1/2}\right]. \tag{4.11}$$

Figure 16 shows the normalized slope $(ak)/(ak)_o$ *vs.* U/c_o, with blocking occurring at $U/c_o = -0.25$ and the slope decreasing monotonically as U/c_o increases, being less than unity for $U/c_o > 0$. According to the geometrical optics approximation, blocking is represented by a singularity that has been interpreted to infer breaking (Mei 1983), but a careful uniformly valid asymptotic analysis of the blockage of linear gravity and gravity–capillary waves by Shyu & Phillips (1990) shows that reflection may occur, although nonlinear effects may still lead to breaking. In any event, the effect of blockage is to significantly exclude waves beyond the blockage point. For waves travelling downstream ($U/c_o > 0$), the slope decreases significantly; by more than an order of magnitude for $U/c_o > 2$.

To quantify these effects we need to estimate the likely values of U/c_o in the ocean. Work by Ding & Farmer (1994), Melville (1994), Terray *et al.* (1996), and most recently Phillips *et al.* (2001), suggests that the mode of the distribution of breaking waves corresponds to waves having phase speeds approximately 60% of the phase speed at the peak of the spectrum, C_p. Now, for a fully developed sea, C_p is comparable to U_{10}, the wind speed at 10 m. Thus we take C, the phase speed of the breaking wave, to be $0.6U_{10}$. How do we characterize the short waves that provide the surface roughness? Following Phillips (1985, pp. 524–525), we take the lower-limit of the phase speed in the gravity equilibrium range, which is of order u_*^a, where u_*^a is

the friction velocity in the air. The drag coefficient, which is $O(10^{-3})$, is defined to be $(u_*^a/U_{10})^2$, so that (U_{10}/u_*^a) and C/c_o are both $O(10)$. Our data show that the surface velocity (normalized by C) is $O(10^{-1}$–$10^{-2})$ for times out to 50 wave periods. Thus, in the field, $|U/c_o|$ could be $O(10^{-1}$–$1)$, and both blockage and significant reductions in the short-wave slope together would combine to leave a smoother surface at the site of the breaker. This would recover to its ruffled wind-driven state by both the local generation of short wind-waves and decay of the induced surface velocity.

On shorter time scales, of the order of the breaking wave period (Lamarre & Melville 1991), we expect that rising plumes of bubbles will lead to regions of divergence and convergence of the surface-velocity field. This too may lead to interactions between short waves and surface currents that both enhance and suppress the waves.

5. Conclusions

We have shown that an overall description of the turbulence and coherent structures generated by breaking waves in the laboratory can be studied using a mosaic of smaller DPIV images. The advances in imaging systems since these experiments were conducted would permit a finer resolution of the velocity field with fewer fields of view, but it is likely that this mosaic approach will still be required to fully represent the flows associated with breaking waves of large Reynolds numbers.

We find that the coherent vortex generated by the breaking wave advects slowly in the wave propagation direction with a speed of approximately $0.01C$, for at least 50 periods after breaking. This is consistent with the speed induced by an image line vortex above the free surface. The speed of the vortex corresponds to the speed at which the fields of turbulent kinetic energy and vorticity propagate downstream. We show that this vortex, through well-established mechanisms of wave–current interaction, may lead to a persistent region of smooth water at the site of breaking in the field.

Our measurements of the kinetic energy and vorticity, and the Reynolds stress, show that they decay as t^{-1}, consistent with the earlier measurements of RM and the recent numerical modelling by Chen *et al.* (1999). Measurements of the Reynolds stress, along with the hypothesis of Reynolds number independence for large R, can be used to estimate the momentum flux from breaking waves into the water column. These estimates are consistent with our earlier measurements described in Melville (1994), but are an order of magnitude less than those implied by the quasi-steady breaking measurements of Duncan (1981, 1983), and an order of magnitude larger than those estimated by Phillips *et al.* (2001) on the basis of field measurements of microwave scattering by breaking waves. These discrepancies must be resolved.

In Appendix A, we show that the DPIV measurements of the kinematics of the flow, which lead to estimates of the dissipation rate and the motion of the coherent vortex downstream, are consistent with independent measurements using a coherent acoustic Doppler technique. Details of the latter technique are presented in Veron & Melville (1999).

In Appendix B, we present measurements of a majority of the terms in the equation for the turbulent kinetic energy. These experiments were not designed to resolve all of these terms so the results should be used with consideration of that fact; however, they suggest that in this statistically unsteady turbulent field, there is a balance between advection of turbulence by the mean flow and vertical transport by the turbulence. Coherent structures and mean flows generated by breaking waves, while readily identified in the laboratory, may be very difficult to isolate in the

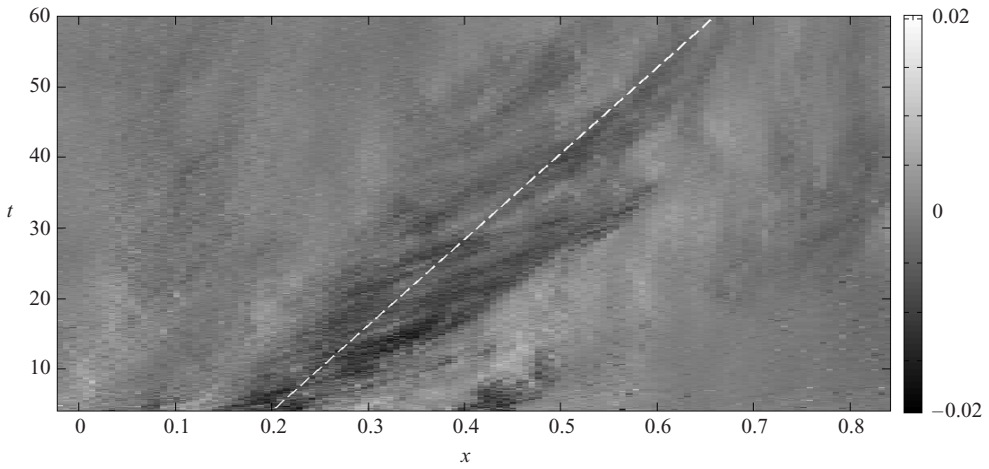

FIGURE 17. $x-t$ diagram of the streamwise velocity measured with a pulse-to-pulse coherent Doppler sonar at a depth of 10 cm looking upstream towards the oncoming wave. The 'structure' near the centre of the figure corresponds to the turbulent eddy moving slowly downstream as seen in figure 9. The dashed line corresponds to the estimate of the propagation speed of $0.013\,\mathrm{m}^{-1}$ based on the DPIV data.

field, and so care must be taken in using the results of measurements like this for modelling breaking in the field. However, these measurements already may provide sufficient insight to permit more detailed modelling of the turbulence generated by breaking waves and its role in heat, gas and momentum transfer across the air–sea interface.

We are grateful for the support of this work by grants from the National Science Foundation (OCE 95-05628, 98-12182) and the Office of Naval Research (Physical Oceanography). We thank Charley Coughran and his team at the Hydraulics Laboratory of Scripps Institution of Oceanography for their support in building equipment and maintaining the facilities. Rob Shear's assistance with the initial DPIV experiments on breaking waves is greatly appreciated. We thank two anonymous reviewers for comments that have improved the final version of the paper.

Appendix A. Comparisons with the acoustic measurements of Veron & Melville (1999)

Veron & Melville (1999, hereinafter referred to as VM) used this same type of breaking-wave flow to test a single-beam pulse-to-pulse coherent acoustic Doppler instrument operating at 1.7 MHz for use in ocean measurements of turbulence. In making those tests, it became clear that the acoustic instrument offered an independent measurement of the kinematics of this laboratory flow. Briefly, the acoustic Doppler instrument was pointed upstream, giving measurements of the horizontal velocity in a measuring volume of 2.5 cm diameter out to a range of 1.5 m, with a range resolution of 1.05 cm. Details may be found in VM.

Figure 17 shows one realization of the streamwise velocity after breaking, as a function of time and range along the channel, at a depth of 0.1 m. The most prominent feature of the figure is a 'structure' propagating downstream in the range $x \approx 0.2-0.6$. This is the vortex that survives the ensemble averaging of the DPIV data

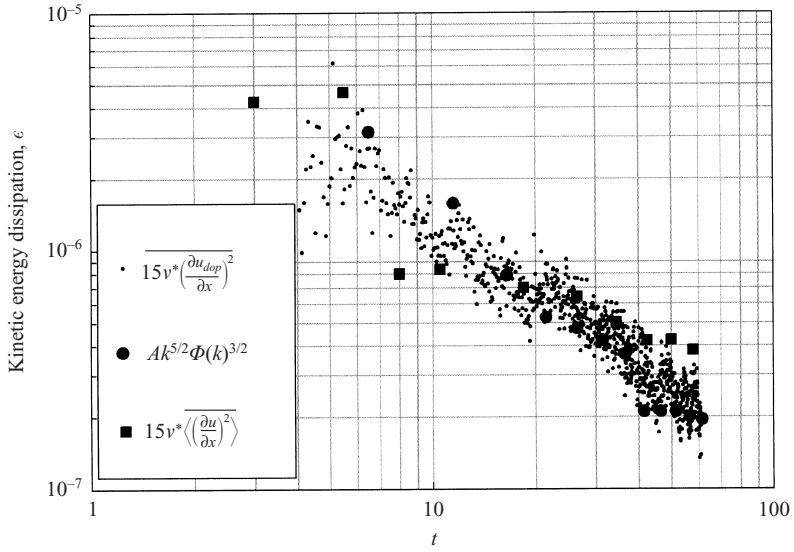

FIGURE 18. Estimates of the dissipation rate ϵ using DPIV measurements and the acoustic Doppler measurements of Veron & Melville (1999). The DPIV estimates are based on strain-rate measurements whereas the acoustical measurements use both strain-rate and inertial subrange estimates. Differences between the three estimates are within the scatter of the data. $\nu*$ is the non-dimensional kinematic viscosity.

(cf. figure 9). The dashed line in the figure corresponds to a velocity of $0.013\,\mathrm{m\,s^{-1}}$, consistent with the induced velocity of the vortex from the optical data.

The acoustical data can be used to infer the dissipation from the amplitude of the inertial subrange in the wavenumber spectrum of the radial velocity field, and from the mean square strain rate of the velocity. These estimates require an assumption of isotropy. Figure 12 shows that the TKE in the streamwise component is at most 50% greater than that in the vertical component, so the r.m.s. velocities differ by at most 25%. Figure 18 shows the isotropic estimates of the dissipation rate, ϵ, estimated from the inertial subrange of the acoustic measurements of the velocity wavenumber spectrum, and rate-of-strain estimates from both the acoustic and DPIV data. Over the range of dissipation rates shown in figure 18, 2×10^{-7}–$5 \times 10^{-6}\,\mathrm{m^2\,s^{-3}}$, the Kolmogorov microscale, η, is in the range 1.5×10^{-3}–$0.67 \times 10^{-3}\,\mathrm{m}$; the dimensionless wavenumber resolved with the DPIV measurements, $\kappa\eta|_{DPIV}$, is in the range 1.6–0.7; and the corresponding dimensionless wavenumber for the acoustical data, $\kappa\eta|_{ac}$, in the range 0.8–0.4. From Tennekes & Lumley (1972 chap. 8), we expect that cutoff wavenumbers in these ranges will lead to good approximations to the total dissipation rate. This conclusion is supported by the fact that the inertial subrange estimates of ϵ, which do not depend strongly on the Nyquist (cutoff) wavenumber, are, within the scatter of the data, consistent with the strain-rate estimates, which do.

Appendix B. The turbulent kinetic energy balance

As discussed in the main body of the paper, these experiments were not designed to undertake a high-resolution investigation of the turbulence generated by breaking, but rather to give an overview of the post-breaking evolution of the velocity field as a prelude to more detailed investigations. In the course of data analysis it became

apparent that some of the terms in the turbulent kinetic energy equation could be evaluated with sufficient precision to compare the order of magnitude of the various terms. This conclusion is supported by the independent estimates of the dissipation presented in Appendix A. So, in the interest of gaining some insight into the kinetic energy balance, perhaps at the expense of accuracy, we present estimates of most of the terms in the TKE equation.

Assuming that the fluid is homogeneous (i.e. stratification by bubbles is negligible) the turbulent kinetic energy equation is (Tennekes & Lumley 1972)

$$\frac{\partial}{\partial t}(\tfrac{1}{2}\langle u_i u_i\rangle) + U_j \frac{\partial}{\partial x_j}(\tfrac{1}{2}\langle u_i u_i\rangle)$$
$$= -\frac{\partial}{\partial x_j}\left(\frac{1}{\rho}\langle u_j p\rangle + \tfrac{1}{2}\langle u_i u_i u_j\rangle - 2\nu\langle u_i s_{ij}\rangle\right) - \langle u_i u_j\rangle S_{ij} - 2\nu\langle s_{ij}s_{ij}\rangle,$$

where the angle brackets, as do the capitals, denote an ensemble average, s_{ij} is the fluctuating rate of strain

$$s_{ij} = \frac{1}{2}\left(\frac{\partial u_i}{\partial x_j} + \frac{\partial u_j}{\partial x_i}\right), \tag{5.1}$$

and S_{ij} is the strain rate of the ensemble-averaged field.

Since we are only measuring two components of the velocity and not measuring the pressure, we cannot provide measured values of all the terms in this equation. Furthermore, we only present the horizontal integrals of those terms over the patch of turbulence generated by the breaking. In this case, the integral of the horizontal turbulent transport term goes to zero and the remaining terms are:

$$\text{evolution:} \qquad \frac{\partial\overline{\langle q\rangle}}{\partial t} \tag{5.2}$$

$$\text{advection:} \qquad \overline{U\frac{\partial\langle q\rangle}{\partial x}} + \overline{W\frac{\partial\langle q\rangle}{\partial z}} \tag{5.3}$$

$$\text{turbulent transport:} \qquad -\frac{\partial}{\partial z}\overline{\langle qw\rangle} \tag{5.4}$$

$$\text{production:} \quad -\overline{(\langle uu\rangle - \langle ww\rangle)\frac{\partial U}{\partial x}} + \overline{\langle uw\rangle\left(\frac{\partial U}{\partial z} + \frac{\partial W}{\partial x}\right)} \tag{5.5}$$

$$\text{dissipation:} \qquad 15\nu\overline{\left\langle\left(\frac{\partial u}{\partial x}\right)^2\right\rangle} \tag{5.6}$$

where the overbar represents the horizontal integral. The turbulent dissipation is represented by the isotropic estimate, and q is set to $\frac{3}{2}\overline{\langle 1/2(u^2+w^2)\rangle} = \frac{3}{2}E_t$ to account for the transverse turbulence which is not measured.

We only consider these terms in the interval between $t = 3$ and 5, since the evolution term can be well represented by differencing over this time interval and the individual terms are sufficiently above the noise to give some insight into the flow. The results of this calculation are shown in figure 19. The most striking feature of this figure is the approximate balance between the advective terms due to the coherent ensemble averaged velocities and the vertical transport of the turbulent kinetic energy by the vertical component of the turbulence. This implies that these terms make no net contribution to the balance of the turbulent kinetic energy. However, we have not

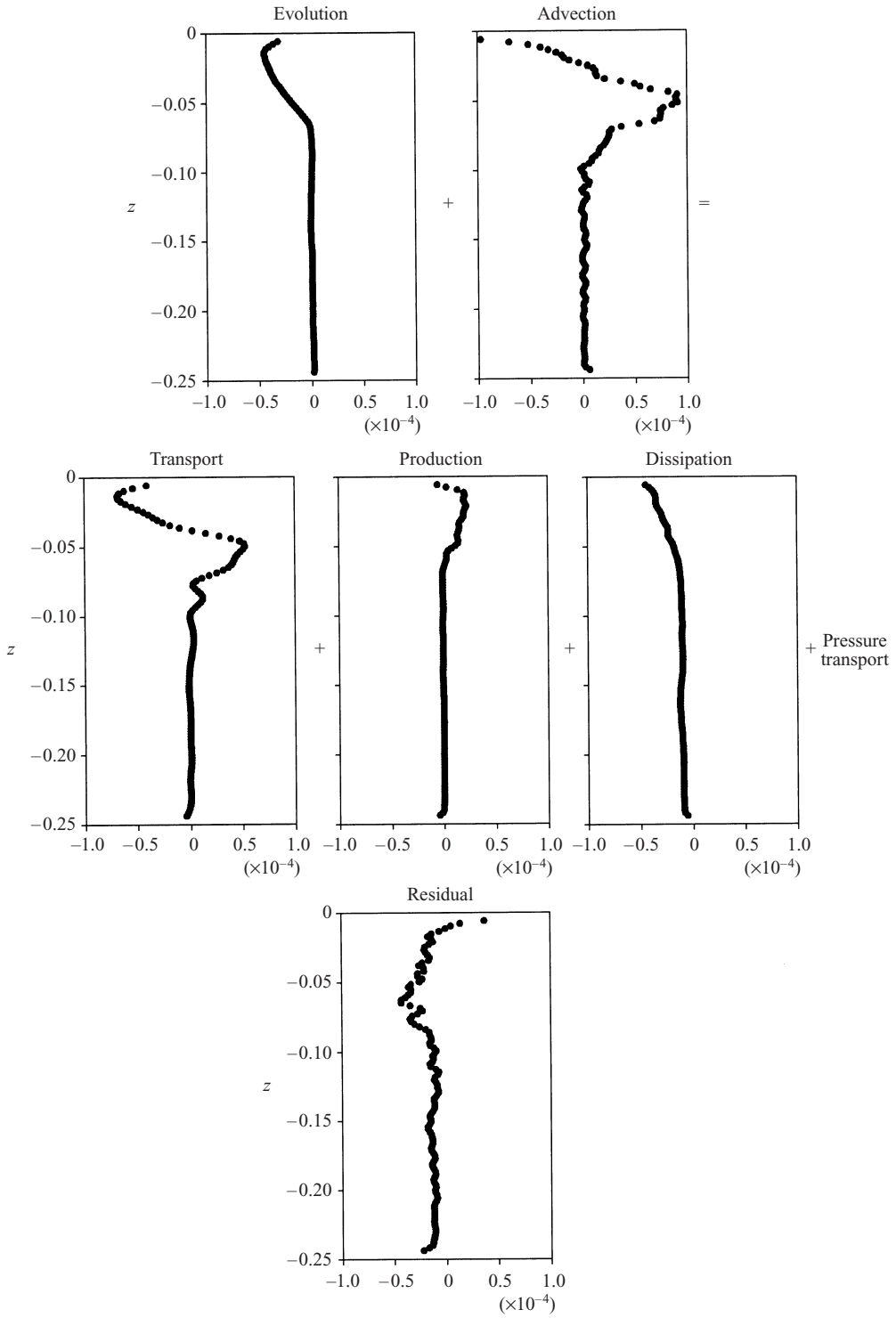

FIGURE 19. Estimates of the terms in the equation for the turbulent kinetic energy, excluding the pressure transport term. The sum of the terms (when all are transposed to the right-hand side of the equation) is also shown. Note the approximate balance between advection and transport.

measured the pressure transport term, so there may not be a complete balance between turbulent transport and advection by the coherent velocity field. The remaining terms, evolution, production and dissipation, also appear to be in approximate balance.

The currently accepted modelling of the steady-in-the-mean wave boundary layer (Craig & Banner 1994; Craig 1996) suggests that it differs from the law-of-the-wall by the predominant balance being between turbulent transport and dissipation rather than production and dissipation, where the transport is associated with turbulence injected by breaking. Now in the field, the measurements are currently unable to distinguish between the coherent breaking-induced mean velocity and the turbulence, and we have considered only the balance of the turbulent kinetic energy, so there may be no inconsistency; however, these results although tentative, do give reasons to consider carefully the implications of measurements like these for modelling of the wave boundary layer.

REFERENCES

Banner, M. L. & Peregrine, D. H. 1993 Wave breaking in deep water. *Annu. Rev. Fluid Mech.* **25**, 373–397.

Chang, K.-A. & Liu, P. L.-F. 1998 Velocity, acceleration and vorticity under a breaking wave. *Phys. Fluids* **10**, 327–329.

Chang, K.-A. & Liu, P. L.-F. 1999 Experimental investigation of turbulence generated by breaking waves in water of intermediate depth. *Phys. Fluids* **11**, 3390–3400.

Chen, G., Kharif, C., Zaleski, S. & Li, J. 1999 Two-dimensional Navier–Stokes simulation of breaking waves. *Phys. Fluids* **11**, 121–133.

Craig, P. D. 1996 Velocity profiles and surface roughness under breaking waves. *J. Geophys. Res.* **101**, 1265–1277.

Craig, P. D. & Banner, M. L. 1994 Modelling wave-enhanced turbulence in the ocean surface layer. *J. Phys. Oceanogr.* **24**, 2546–2559.

Ding, L. & Farmer, D. M. 1994 Observations of breaking surface wave statistics. *J. Phys. Oceanogr.* **24**, 1368–1387.

Duncan, J. H. 1981 An experimental investigation of breaking waves produced by a towed hydrofoil. *Proc. R. Soc. Lond.* A **377**, 331–348.

Duncan, J. H. 1983 The breaking and non-breaking wave resistance of a two-dimensional hydrofoil. *J. Fluid Mech.* **126**, 507–520.

Duncan, J. H., Philomin V., Behres, M. & Kimmel, J. 1994 The formation of spilling breaking water waves. *Phys. Fluids* **6**, 2558–2560.

Duncan, J. H., Qiao, H., Philomin, V. & Wenz, A. 1999 Gentle spilling breakers: crest profile evolution. *J. Fluid Mech.* **379**, 191–222.

Fedorov, A. V. & Melville, W. K. 1998 Nonlinear gravity–capillary waves with forcing and dissipation. *J. Fluid Mech.* **354**, 1–42.

Fedorov, A. V., Rozenberg, A. & Melville, W. K. 1998 An experimental and numerical study of parasitic capillary waves. *Phys. Fluids* **10**, 1315–1323.

Lamarre, E. & Melville, W. K. 1991 Air entrainment and dissipation in breaking waves. *Nature* **351**, 469–472.

Lin, J. C. & Liu, P. L.-F 1999 A numerical study of breaking waves in the surf zone. *J. Fluid Mech.* **359**, 239–264.

Lin, J. C. & Rockwell, D. 1995 Evolution of a quasi-steady breaking wave. *J. Fluid Mech.* **302**, 29–44.

Loewen, M. R. & Melville, W. K. 1991 Microwave backscatter and acoustic radiation from breaking waves. *J. Fluid Mech.* **224**, 601–623.

Mei, C. C. 1983 *Applied Dynamics of Ocean Surface Waves*. Wiley.

Melville, W. K. 1994 Energy dissipation by breaking waves. *J. Phys. Oceanogr.* **24**, 2041–2049.

Melville, W. K. 1996 The role of wave breaking in air–sea interaction. *Annu. Rev. Fluid Mech.* **28**, 279–321.

Melville, W. K., Shear, R. & Veron, F. 1998 Laboratory measurements of the generation and evolution of Langmuir circulations. *J. Fluid Mech.* **364**, 31–58.

Melville, W. K., White, C., Veron, F. & Luft, E. 1999 Laboratory measurements of turbulence under breaking waves. In *The Wind-Driven Air–Sea Interface: Electromagnetic and Acoustic Sensing, Wave Dynamics and Turbulent Fluxes* (ed. M. L. Banner), pp. 211–218. University of New South Wales.

Phillips, O. M. 1985 Spectral and statistical properties of the equilibrium range in wind-generated gravity waves. *J. Fluid Mech.* **156**, 505–531.

Phillips, O. M., Posner, F. L. & Hansen, J. P. 2001 High range resolution radar measurements of the speed distribution of breaking events in wind-generated ocean waves: surface impulse and wave energy dissipation rates. *J. Phys. Oceanogr.* **31**, 450–460.

Rapp, R. J. & Melville, W. K. 1990 Laboratory measurements of deep-water breaking waves. *Phil. Trans. R. Soc. Lond.* A **331**, 735–800.

Shyu, J.-H. & Phillips, O. M. 1990 The blockage of gravity and capillary waves by longer waves and currents. *J. Fluid Mech.* **217**, 115–141.

Tennekes, H. & Lumley, J. L. 1972 *A First Course in Turbulence*. MIT Press.

Terray, E. A., Donelan, M. A., Agrawal, Y. C., Drennan, W. M., Kahma, K. K., Williams, A. J., Hwang, P. A. & Kitaigorodskii, S. A. 1996 Estimates of kinetic energy dissipation under breaking waves. *J. Phys. Oceanogr.* **26**, 792–807.

Terrill, E., Melville, W. K. & Stramski, D. 1998 Bubble entrainment by breaking waves and their effects on the inherent optical properties of the upper ocean. In *Proc. of Ocean Optics OOXIV, Kona, HI, November 1998*, 11 pp.

Terrill, E., Melville, W. K. & Stramski, D. 2001 Bubble entrainment by breaking waves and their influence on optical scattering in the upper ocean. *J. Geophys. Res.* **106** C8, 16 815–16 824.

Veron, F. & Melville, W. K. 1999 Pulse-to-pulse coherent Doppler measurements of waves and turbulence. *J. Atmos. Oceanic Tech.* **16**, 1580–1597.

White, C. J. 1996 A laboratory study of breaking waves using digital particle image velocimetry. MS thesis, University of California, San Diego.

Willert, C. E. 1992 The interaction of modulated vortex pairs with a free surface. PhD thesis, University of California, San Diego.

Willert, C. E. & Gharib, M. 1991 Digital particle image velocimetry. *Exps. Fluids* **10**, 181–193.